Iceberg Detection With RADARSAT-2 Quad-Polarimetric *C*-Band SAR in Kongsfjorden, Svalbard—Comparison With a Ground-Based Radar

Johnson Bailey, *Member, IEEE*, Vahid Akbari, Tao Liu, *Member, IEEE*, Tom Rune Lauknes, *Member, IEEE*, and Armando Marino, *Member, IEEE*

***Abstract*—Satellite monitoring of icebergs in the Arctic region is paramount for the safety of shipping and maritime activities. The potential of polarimetric synthetic aperture radar data in enhancing detection capabilities of icebergs under interchangeable and challenging conditions is explored in this work. We introduce RADARSAT-2 quad-pol *C*-band data to detect icebergs in Kongsfjorden, Svalbard. The location contains two tidewater glaciers and is chosen because multiple processes are present in this region, such as ice formation and its relationship with the glaciers, freshwater discharge. Six state-of-the-art detectors are tested for detection performance. These are the dual-intensity polarization ratio anomaly detector, polarimetric notch filter, polarimetric match filter, symmetry, polarimetric whitening filter (PWF), and optimal polarimetric detector (OPD). In addition, we also tested the parameters of the Cloude–Pottier decomposition. In this study, we make use of a ground-based radar for validation and comparison with satellite images. We show that in calm sea-state conditions, the OPD and PWF detectors give high probability of detection (P_D) values of 0.7–0.8 when the probability of false alarm (P_F) value is 0.01–0.05, compared with choppy sea conditions where the same detectors have degraded performance ($P_D = 0.5$–0.7). Target-to-clutter ratio (TCR) values for each polarization channel is also extracted and compared to the icebergs' dimensions. The ground-based radar shows higher values in TCR, compared with satellite images. These findings corroborate previous work and show that sea-ice activity, surface roughness, incidence angle, weather, and sea-state conditions all affect the sensitivity of the detectors for this task.**

***Index Terms*—Classification, detection, ground-based radar, icebergs, polarimetry, synthetic aperture radar (SAR).**

I. Introduction

ICEBERGS are major hazards to maritime activities in the Arctic region [1]. Synthetic aperture radar (SAR) satellites can help identify icebergs and are particularly useful in this region due to the ability to penetrate cloud cover and provide images at night time [2], [3], [4], [5], [6], [7], [8], [9], [10]. In this work, target detection algorithms are applied to three RADARSAT-2 (RS2) images of an area of iceberg and sea-ice cover in the Kongsfjorden in Svalbard, Norway. In Kongsfjorden, icebergs and growlers are calving off the Kronebreen and Kongsbreen tidewater glaciers and may become embedded within sea-ice floes in winter [11]. Often, these icebergs become trapped within the fjord and may not escape for months or even years. The fjord presents multiple changing processes, including wind, freshwater discharge, and seasonal ice formation. The location is also chosen due to the variety of environmental conditions, such as sea states, sea-ice types, and freezing and melting conditions of glacial ice. Icebergs in this region tend to have a small size $<$120 m in length and are often irregular in shape, compared with their Antarctic counterparts [12], [13], [14], [15], [16].

The detection of icebergs using SAR data often employs conventional constant false alarm rate (CFAR) using a sliding window. Targets are discriminated by looking at anomalies in the backscattering when comparing a target window with a clutter window [17]. The threshold is set using statistical tests and any target brighter than the threshold triggers a detection. Thus, this technique helps to identify bright targets in darker clutter background. However, when using a CFAR approach, numerous problems arise. First, it is very common for the ocean clutter window to become contaminated by nearby targets [18]. In areas of high iceberg density, such as at the edge of glacier tongues, the large presence of icebergs can disrupt the statistical modeling of clutter, causing severe reduction in CFAR detection performance. This is known as the capture effect [19]. Second, the meteorological and oceanographic conditions, including presence of sea ice, can increase the backscatter from the sea, causing heterogeneous clutter and, thus, higher false alarm rates. This is known as the clutter edge effect [20]. Third, the size of the window being used is important; bigger windows can include more image pixels, diluting targets during averaging, while smaller windows can exclude pixels of iceberg edges and present more speckle noise. Attempts to address these problems include the implementation of a guard window in between the testing and training windows, which has been shown to increase performance [21]. Another limitation to these iceberg detection methods is that even in areas, such as open ocean, numerous rocks and small islands can increase the number of false alarms. This is addressed by including an initial stage

Manuscript received 3 November 2023; revised 8 January 2024; accepted 9 February 2024. Date of publication 26 February 2024; date of current version 8 March 2024. *(Corresponding author: Johnson Bailey.)*

Johnson Bailey, Vahid Akbari, and Armando Marino are with the University of Stirling, FK9 4LA Stirling, U.K. (e-mail: johnson.bailey@stir.ac.uk; vahid.akbari@stir.ac.uk; armando.marino@stir.ac.uk).

Tao Liu is with the The Naval University of Engineering, Wuhan 430030, China (e-mail: liutao1018@hotmail.com).

Tom Rune Lauknes is with the NORCE Norwegian Research Centre AS, Siva Innovasjonssenter, 9294 Tromsø, Norway (e-mail: tlau@norceresearch.no).

Digital Object Identifier 10.1109/JSTARS.2024.3369392

in image processing in which a land mask is applied before detection can begin [22]. In general, when using any land mask, it would be important to consider if the mask being used has small, unmapped rocks and features; in that case land targets can be removed by using time series (i.e., observing the target stable over many years).

It is well known that polarimetric synthetic aperture radar (PolSAR) can help target classification and, therefore, the discrimination between icebergs and background. Multiple articles highlight the importance of cross polarization; icebergs tend to be detected easier in the HV channel compared with copolarization channels HH and VV due to the reduced cross-pol backscattering of the surface clutter [4], [23], [24]. When it comes to icebergs, this finding was also shown by Dierking and Wesche [4].

Previous work undertaken in Kongsfjorden has utilized *C*-band PolSAR. Akbari and Brekke [25] proposed a near-real-time processing chain for iceberg detection in nonhomogeneous areas of sea clutter. An iceberg segmentation algorithm was tested on quad-pol RS2 images and found to handle various sea states and areas of high iceberg density. However, it should be noted that the frequency at *C*-band may not be low enough to further discriminate between iceberg and sea-ice backscatter return because *C*-band frequencies will not penetrate far enough in fresh water ice to reveal internal features of iceberg bodies, such as cracks, and crevasses [4].

Previous work has been carried out on the icebergs of a similar size and shape in east and west Greenland [21] using ALOS-2 *L*-band SAR images. Here, several detectors were tested for two scenarios: icebergs in open ocean and icebergs embedded within sea-ice floes. More recently, Himi et al. [26] carried out in locations off the coast of Newfoundland and have concluded that icebergs exhibit a high-volume scattering in open ocean, compared with surface scattering in sea ice. Various limitations, however, still warrant further research. With the calving of 30 000 icebergs a year estimated in the Arctic regions [6], [23], attention now turns to areas situated at glacier termini.

Previous studies in iceberg detection and characterization noted challenges with using consistent ground-truth data, which allows for reliable validation and calibration of detectors obtained from processing satellite data. While ship observations could be used, they are temporally and spatially limited and it is unlikely that a quad-polarimetric image is acquired during a vessel spotting. Therefore, it is of high value to use ground-truth data from remote sensing datasets and in situ observations.

The main contributions of this work are as follows.

1) The application of six state-of-the-art detectors to an RS2 dataset in Kongsfjorden, Svalbard to determine the overall detection performance in this environment. These detectors are the dual-intensity polarization ratio anomaly detector (iDPolRAD), polarimetric notch filter (PNF), polarimetric match filter (PMF), symmetry, optimal polarimetric detector (OPD), and polarimetric whitening filter (PWF). We also make use of Cloude–Pottier entropy for comparison purposes.
2) The validation of the satellite detection results using data acquired from Ku-band ground-based radar.
3) The comparison of the iceberg backscattering between *C*-band RS2 and Ku-band ground-based radar, which we find is dependent on incidence angle range.

One of the novelties of this work is the use of the ground radar: the gamma portable radio interferometer (GPRI) [27], [28]. The ground and satellite images were acquired at the same time allowing direct comparison. GPRI also provides an insight about the more general topic of iceberg detection with radar.

The rest of this article is organised as follows. An introduction to PolSAR is presented in Section II. Methods are reviewed in Section III, and a background to the dataset is introduced in Section IV. Results are presented in Section V. Discussions are outlined in Section VI. Finally, Section VII concludes this article.

II. PolSAR

We present a very brief summary of PolSAR theory. A SAR antenna can transmit electromagnetic waves in either a linear horizontal or a linear vertical orientation. If a wave is transmitted and received back to the antenna in a horizontal orientation, this is termed HH. The opposite is true for vertically transmitted and received waves known as VV. If we receive the orthogonal orientation, we talk about cross-polarized channels HV and VH. Any single (deterministic) target on the ground can be represented using these four different polarization channels that represent the complex backscattering from the target. We characterize this using the scattering matrix **[S]**

$$[\boldsymbol{S}] = \begin{bmatrix} \mathrm{HH} & \mathrm{HV} \\ \mathrm{VH} & \mathrm{VV} \end{bmatrix}. \tag{1}$$

The matrix can also be represented in the fashion of a scattering vector $\underline{k}$. When the system is monostatic and the medium is reciprocal, the scattering vector, as notated by Cloude [29], can be written as

$$\underline{k} = \begin{bmatrix} \mathrm{HH}\ \sqrt{2}\mathrm{HV}\ \mathrm{VV} \end{bmatrix}^T \tag{2}$$

where ^{T} refers to the transpose. This scattering vector $\underline{k}$ is also known as a lexicographic vector. By changing the representation basis of this vector, we obtain a generic scattering vector

$$\underline{k} = [k_1, k_2, k_3]^T. \tag{3}$$

In this work, we choose this transformation into a Pauli vector in order to apply a physical interpretation of the alpha parameter from the Cloude–Pottier decomposition (see Section III). The Pauli vector is expressed as follows:

$$\underline{k} = \frac{1}{\sqrt{2}}[\mathrm{HH} + \mathrm{VV}\ \mathrm{HH} - \mathrm{VV}\ 2\mathrm{HV}]^T. \tag{4}$$

A. Cloude–Pottier Decomposition

The classification of partial targets has been widely carried out using the Cloude–Pottier decomposition, which considers a diagonalization of **[T]**. This is a Hermitian matrix and, therefore, has positive eigenvalues and orthogonal eigenvectors. **[T]** can be

decomposed into the following:

$$[T] = \lambda_1 \underline{e_1 e_1^{*T}} + \lambda_2 \underline{e_2 e_2^{*T}} + \lambda_3 \underline{e_3 e_3^{*T}} \quad (5)$$

where λ_i are the eigenvalues and $\underline{e_i}$ are the eigenvectors. The eigenvectors can be written as follows:

$$\underline{e_i} = e^{i\phi_i} \left[\cos\alpha_i \;\; \sin\alpha_i \cos\beta_i e^{i\delta_i} \;\; \sin\alpha_i \sin\beta_i e^{i\gamma_i}\right]^T. \quad (6)$$

From here, we extract the entropy parameter [29], which we utilize as a detector.

III. Methods

We use quad-pol RS2 images to identify icebergs in surrounding sea-ice clutter. The iceberg detection system in this article consists of the following processing steps.

A. Preprocessing

The preprocessing was carried out using the processing stack of CIRFA Center UiT-The Arctic University of Norway, which provided the data already in a multilooked format for this study. The raw data were extracted and calibrated as sigma nought. They produced the covariance matrix elements of each acquisition and converted into a coherency matrix by using a unitary transformation matrix. Geocoding was applied to the elements of the coherency matrix.

B. Masking

To reduce the possibility of false alarms caused by radar backscatter from islands and rocks in the fjord, a land mask is applied by using a land boundary map or shoreline layer. However, land masking is not always fully accurate due to multiple factors. These include geocoding errors, errors in recording coastline, unmapped rocks, erosion of coastline, and variations in tides [31]. The land mask we use here was provided by the Norwegian Polar Institute (NPI).

C. Preparing Validation Dataset

In order to validate the detectors, we identified areas of open ocean, sea ice, and icebergs.

The creation of the validation dataset is achieved by extracting the ground-based images, and then in both the satellite and ground datasets, applying polygons to each set of pixels that are visually identified as an iceberg. Icebergs are selected if they appear very bright in the image, cast a shadow to the side, and are not rectangular in shape (which may indicate a vessel). We extract the center coordinates for each iceberg, as well as the size.

In the following, we produce a shapefile of clutter polygons as a secondary layer, and then merge and stack layers together. We also produce target and clutter masks from the RS2 scenes (see Fig. 4).

Finally, all the satellite and ground raster data were stacked together to form a final data cube. The final raster cube consists of all three acquisitions, the masks for target, clutter, and land mask, and ground image raster data.

D. Detectors

We outline a very brief review of all the detectors used in this work. In addition, for comparison, we applied thresholds to the Cloude–Pottier parameters described in Section II, turning them into detectors.

1) iDPolRAD: Introduced and proposed by Marino et al. [24], the iDPolRAD detector was used to separate icebergs from sea-ice floes in dual-pol Sentinel-1 SAR images. Based on the intensity of the cross- and copolarization channels VH and VV, it uses a clutter and a target window that runs across the area of interest, such as a boxcar filter.

2) PNF: The PNF is also proposed by Marino [32] to detect ships. It is based on geometrical perturbation analysis and assumes that the sea clutter is homogeneous.

3) PMF: The PMF has previously been used for contrast enhancement in target detection. The PMF was proposed by Novak et al. [33].

4) Reflection symmetry: This detector is applied to the C_{12} element of a covariance matrix, and therefore can be used with quad- or dual-polarimetric data [34] since it uses only the complex values of HH and HV.

5) PWF: The PWF was proposed by Novak and Burl [35] for the reduction of speckle noise in PolSAR images. Effectiveness of this detector depends on the quality of clutter estimation, and we use a multilook PWF in this work proposed by Liu et al. [36].

6) OPD: The OPD is based on the maximum likelihood ratio test (LRT) under complex Gaussian statistics [33], [35]. Considering both the target-to-clutter ratio (TCR) and speckle reduction, the LRT can be derived as long as target and clutter distributions are known.

E. Target-to-Clutter Ratio

In order to detect icebergs in SAR images, a significant level of contrast between target and background clutter is required. Here, we use TCR to evaluate the contrast between icebergs and background clutter for the polarimetric channels C_{11}, C_{22}, C_{33}, T_{11}, and T_{22}. The TCR of each iceberg was calculated by taking the maximum or the mean value of a few iceberg pixels and dividing either by the mean value of the closest clutter area [37], [38]. Note that the concept of TCR requires to have a ratio of powers and, therefore, it cannot be easily extended to other detector observables. This is because the detector observables often receive a nonlinear transformation, which acts on the dynamic range, making them not comparable with power measurements.

It is important to note that the TCR is affected by factors, such as the number of pixels, used for the estimation. In this work, we consider the maximum in a 3×3 window to evaluate TCR statistics

$$\text{Max TCR} = \frac{\text{target}_{\text{max}}}{\text{clutter}_{\text{mean}}} \quad (7)$$

where $\text{target}_{\text{max}}$ is the maximum intensity of the pixels representing each of the icebergs, and $\text{clutter}_{\text{mean}}$ is the mean of the

intensity of the pixels representing the clutter

$$\text{Mean TCR} = \frac{\text{target}_{\text{mean}}}{\text{clutter}_{\text{mean}}} \tag{8}$$

where $\text{target}_{\text{mean}}$ is the mean intensity of the pixels representing each of the icebergs.

F. Visual Identification of Icebergs

In the following, there is an explanation of the rules we used to perform the visual identification of icebergs.

1) *Brightness*: Icebergs in SAR images represent higher brightness than the surrounding ocean. However, sea-ice backscatter intensities can be similar to icebergs [26]. Using brightness alone is not sufficient to identify all icebergs within a high-density region of sea-ice cover. To avoid errors in iceberg identification, it is useful to add information about the geometry and shape.
2) *Longitudinal axis*: We focused on smaller icebergs of less than 120 m in longitudinal length since these are the ones that are harder to detect. The size of the targets we visually identified did not exceed 120 m.
3) *Shadow*: Targets, which are bright on an image with a darker region next to it, are considered as potential icebergs. In sea ice, icebergs can often be identified by their shadow, even if the pixel brightness compared to that of the sea ice is the same.
4) *Shape*: Targets with regular elongated shapes are considered to be vessels and are eliminated from the analysis.

If all the above discrimination features fall within the ranges we specified, the target is considered to be an iceberg. Clearly, when performing this visual identification, we mostly select icebergs surrounded by relatively low sea or sea-ice backscatter brightness levels. The ones embedded in high clutter areas (high sea state and deformed ice) are just not visible with enough confidence. However, the receiver operating characteristic (ROC) curves and TCR compare icebergs with clutter areas that are not necessarily surrounding the iceberg and, therefore, can have larger intensity.

The icebergs are then polygonized so that geometrical properties, such as area, shape, major and minor axis, are made available in tabular form. The area is calculated by counting the pixels that make up each iceberg and multiplying by pixel spacing. The position of an iceberg is determined using the coordinates of the iceberg polygon centroid, which can be converted into latitude and longitude using the geocoded information of the PolSAR image.

G. ROC Curve Analysis

In this work, we assess detector's performance using ROC curves applied to the different detector transformations. That is to say, each detector will produce an image representing the observed strength of the anomaly as seen by that detector. A variable threshold is run for each of these maps and the probability of false alarm (P_F) and the probability of detection (P_D) are measured and plotted (one against the other) while the threshold is varied. We, therefore, do not apply any CFAR detection requiring a single threshold, but we test in a most comprehensive way by trying all the possible thresholds. This ensures that we are not biased by the selection of the pdf for the detector, which may fit some detectors better than others and also be a function of the dataset considered.

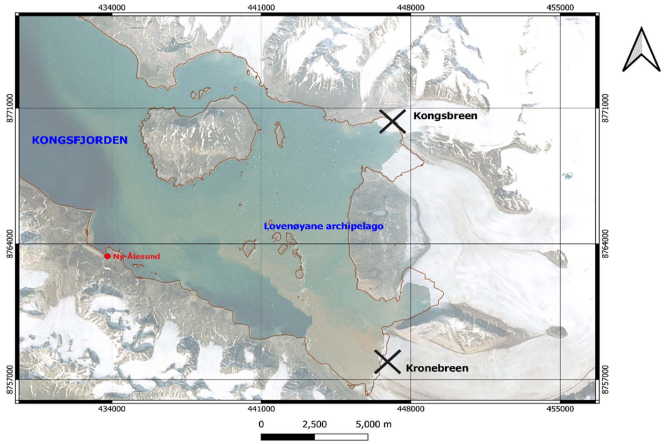

Fig. 1. Study area showing Kongsfjorden in Svalbard, Norway. Black crosses indicate the tidewater glacier termini, red text indicates the settlements, blue text indicates the Kongsfjorden and the Lovenøyane archipelago, and brown line indicates the land masking.

IV. Study Area and Dataset

In this section, we introduce the dataset and summary tables of the satellite and ground radars.

All data were acquired over Kongsfjorden in Svalbard, where iceberg calving is prominent. Kongsfjorden is situated on the west coast of Spitsbergen in Ny Alesund at roughly 79°N and 12°E (see Fig. 1). Radar backscatter is affected by the changing conditions in the fjord since the Kronebreen and Kongsbreen glaciers produce an abundance of icebergs and growlers through calving. This is in addition to freshwater discharge and wind, which, in turn, affects sea-ice activity and changing sea states. Sea-ice activity is most prevalent from September to June, usually in the inner part of the fjord, while the outer part is usually open sea or contains drift ice. Typically, icebergs can be found embedded and stuck within the sea ice during winter months and drifting in open ocean during the summer months [39]. The location is also in close proximity to an NPI research station on the south side of the fjord, which aids in logistics for fieldwork.

Icebergs can also collect and become clustered or grounded within fjords. A fjord is defined as an area where at least 20% of the coastline is dominated by tidewater glaciers [40]. Notable iceberg sizes range from growler to bergy bit. Studies on the size and frequencies of icebergs in the fjord have found that the largest berg was 30 m in width, although it was an outlier. Although this work focuses on icebergs from two tidewater glaciers, the fjord is fed by five glaciers [41]. However, sea-ice floes are also present in the fjord, which makes distinguishing the smallest icebergs from sea-ice floes very difficult. Another significance of Kongsfjorden is that it is rather shallow in areas

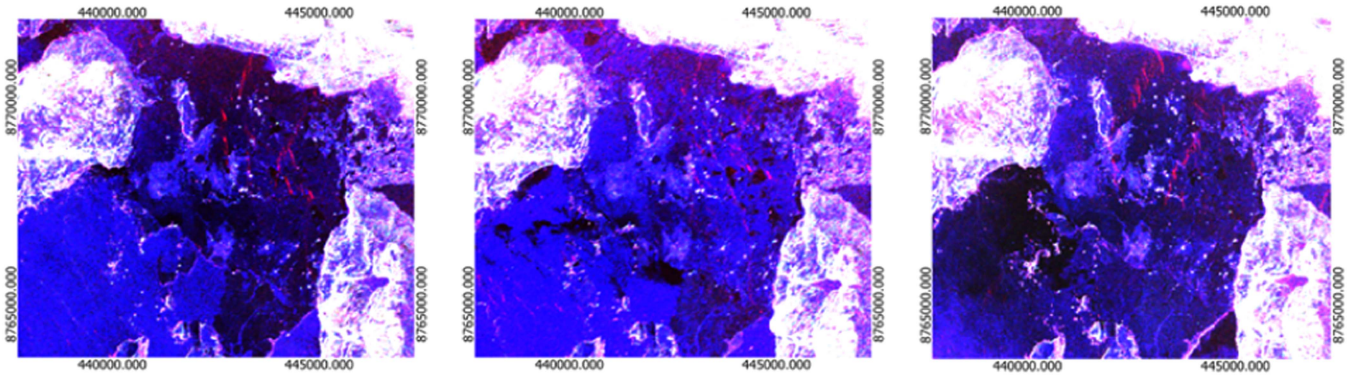

Fig. 2. RS2 Pauli RGB images in coordinates. (a) 15th April. (b) 16th April. (c) 17th April.

TABLE I
RS-2 IMAGE ACQUISITIONS

Scene	*ID*	*Date*	*Time (UTC)*	*Lat/Lon*	*Beam*	*Incidence Angle (°)*	*Orbit*
20160415	*470697*	*15th April*	*15:39*	*12.340636, 78.924756*	*FQ13*	*32–34*	*Asc*
20160416	*470930*	*16th April*	*15:10*	*12.328320, 78.932074*	*FQ5*	*23–25*	*Asc*
20160417	*471190*	*17th April*	*15:10*	*12.175653, 78.896132*	*FQ25*	*38–40*	*Asc*

Note that the latitude and longitude are for the center coordinate of each scene.

TABLE II
GPRI SPECIFICATIONS

Frequency (GHz)	*Operational Range (m)*	*Range Resolution at 1 km distance (m)*	*Azimuth Resolution at 1 km distance (m)*	*Transmit bandwidth (MHz)*	*Time*
17.1–17.3	20–10 000	0.95	6.8	200	15–17 April

where icebergs are drifting. Only 26% of the inner fjord in Kongsfjorden has a depth more than 20 m. This would mean that, in the other 74% of the inner fjord, many icebergs can become grounded and end up melting in the fjord in less than a month. It is also suggested that most of the icebergs come from Kronebreen, as it is a relatively fast flowing glacier and is also highly crevassed, which suggests more smaller size calving of irregular shape icebergs [42].

For this analysis, a total of 92 icebergs were selected for analysis using satellite data, and a total of 60 icebergs were selected for data validation using the ground radar.

A. RADARSAT-2

The satellite data in this article consist of three quad-pol *C*-band SAR images in fine beam mode acquired from the CIRFA Center UiT-The Arctic University of Norway [43]. As listed in Table I, the SAR scenes were taken with both ascending orbits and an incidence angle range of 23°–46°. All RS2 images were acquired as single-look complex (SLC) with a resolution of 5.2 m × 7.6 m in slant range and azimuth dimensions, respectively. They cover the time span between 15 and 17 April 2016. The images were calibrated, multilooked, and geocoded to a Universal Transverse Mercator grid to produce images with 20 m pixel spacing. Therefore, the final resolution for the images used in this study is 20 × 20. Fig. 2 shows the geocoded Pauli RGB (R = HH−VV, G = HV, and B = HH+VV) of the acquisitions. The scene collected on 15th April [see Fig. 2(a)] shows a relatively calm sea state with sea-ice present west of the Lovenøyane archipelago. The open sea north of the archipelago has an extremely low radar backscatter, representing a very calm sea state, and this is where the icebergs are more visible. The scene collected on 16th April [see Fig. 2(b)] appears to show a more heterogeneous sea state due to higher wind conditions.

When compared with Fig. 2(a), icebergs north of the Kronebreen glacier appear to be drifting northwest. Brighter iceberg backscatter signatures are also visible. The scene collected on 17th April [see Fig. 2(c)] shows a relatively calmer sea. The sea appears calmer than in Fig. 2(b), as shown by less bright radar backscattering. The icebergs west of the Kongsbreen glacier appear to show higher backscatter. This can be attributed to a higher incidence angle in comparison to the first two scenes. In all images, the majority of icebergs are situated slightly north east of the archipelago, while the outer part of Kongsfjorden appears to be free of icebergs.

B. Gamma Portable Radio Interferometer

Ground-based data used in this work consist of three real aperture Ku-band (1.74 wavelength) GPRI image acquisitions with a ground azimuth resolution of roughly 7 m (in the location of the icebergs) at 1 km distance and a range resolution of roughly 1 m in Table II. Beginning on 15th April at 15:15 (UTC time), the instrument conducted a sweep every 2 min with only one interruption of 4 h on the morning of 16th April, and continued until 19th April at 08:00. The three images in question were collected on 15th April until 17th April and have corresponding times with the RS2 data. The GPRI data are used in two ways: as ground truth for the satellite data to visually identify icebergs, and to compare the detectability of icebergs in the two systems.

TABLE III
METEOROLOGICAL DATA FROM NY-ÅLESUND WEATHER STATION

Image	Temperature (°C)	Wind Speed (m/s)	Wind Direction
20150415	−10	5.4	SE
20150416	−7.5	1.7	SSE
20150417	−7.1	7.3	ESE

Full coverage of data is available from YR, a service from the Norwegian Meteorological Institute and NRK (https://www.yr.no/nb).

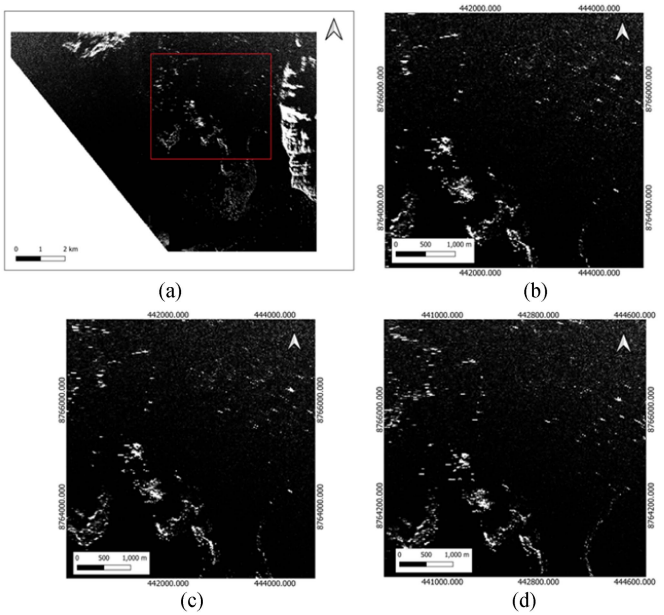

Fig. 3. GPRI scene acquisition GIS coordinates. (a) Full image. (b) Zoom 15th April. (c) Zoom 16th April. (d) Zoom 17th April.

The large extent of the images generated from the GPRI, together with the high frequency and quality of the intensity images, demonstrate the potential of using ground-based radar observations to identify and characterize icebergs and growlers.

Fig. 3 shows the ground-radar scene from 15th April, together with smaller region of interest (ROI) in each of the three acquisitions in order to have a closer look in the areas we can visually identify icebergs. The larger contrast can be attributed to a higher incidence angle in each scene or with the difference in frequency. It is important to note that, due to these differences, icebergs that are visible in ground images may not be visible in satellite images.

C. Meteorological Conditions

Meteorological data covering temperature, wind speed, and direction can be found in Table III. Data are taken from the nearby Ny-Ålesund weather station, and all data correspond to the date and time of each image acquisition. This additional data help with a more robust analysis

V. RESULTS

A. Preliminary Image Analysis

Fig. 4 shows the RS2 target and clutter masks we used for performing validation in each acquisition. Note, between dates, some of the icebergs drifted, and therefore, we needed to derive their masks in different acquisitions.

The SAR images clearly show that the icebergs are drifting in the fjord. The majority of the icebergs are densely concentrated just north of the archipelago, while some clusters are also found further east and north–east.

B. Detector Images

Fig. 5 shows the detector observables in a chosen ROI, as displayed in Fig. 4, covering the area with most targets. These images have been produced before thresholding is applied in order to visualize the detection maps. Here, the validation work was done visually, spotting the icebergs within the images. In this way, it is easier to give a qualitative analysis of detection performance. We do not use lambda2 in this work. Note, all the figures of each detector do not contain units.

Fig. 5 depicts the iDPolRAD, DPolRAD, PNF, and symmetry. From Fig. 5, we can see that the iDPolRAD and symmetry detectors tend to discriminate icebergs from the surrounding clutter, followed by the DPolRAD and notch filter. In the DPolRAD and symmetry detectors, areas of sea ice can also be observed, and it is likely that the number of false alarms will reflect this. However, it is possible to see that some of the icebergs seem to be missing.

Fig. 6 shows detection image outputs for entropy, alpha, and lambda1, lambda3, which are the eigenvalues of coherency matrix **[T]**. From Fig. 6, initially, it is evident that detection performance is lower. In fact, it is very difficult to see icebergs in the entropy and alpha, whereas lambda1 and lambda3 are able to distinguish some icebergs, although these appear brighter in lambda3. Since entropy and alpha are not really used for detection, it is only being used for comparison purposes.

Fig. 7 shows the detection image outputs for OPD, PWF, and PMF. In Fig. 7, the performances of sigma1, PWF, and OPD appear very similar. These are focused on enhancing contrast, and therefore allow a clearer visibility of those. Although these detectors improve contrast, when it comes to detection theory, it is also important to analyze the variation of target and clutter, which impact their separability. We, therefore, need ROC curve analysis.

C. Detector Performance ROCs

In this section, we present the ROC curves, which show the estimated probability of detection (P_D) against the probability of false alarms (P_F) for each detector. Figs. 8 –10 represent an ROC curve for the scene collected on 15th April, 16th April, and 17th April, respectively.

From Fig. 8, we can clearly see that the detection performance is variable across all detectors. The behavior of the detectors

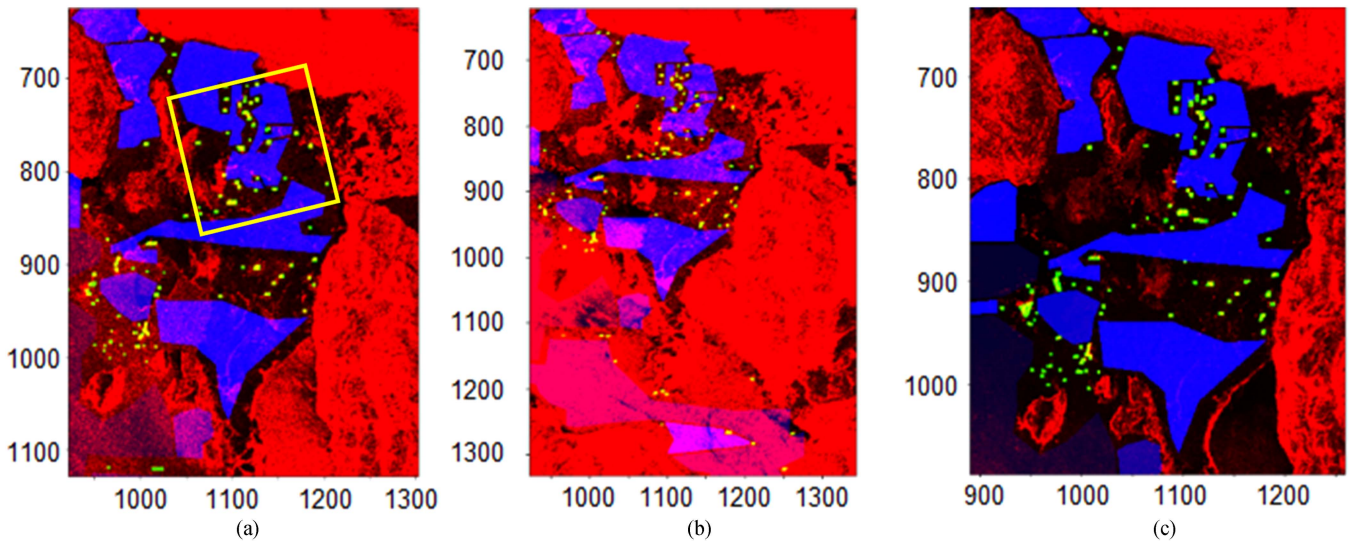

Fig. 4. Target and clutter mask ROI. (a) 15th April. (b) 16th April. (c) 17th April. Blue areas mark the clutter, green/yellow polygons indicate the icebergs, yellow box indicates the detection ROI, and red color indicates the background image.

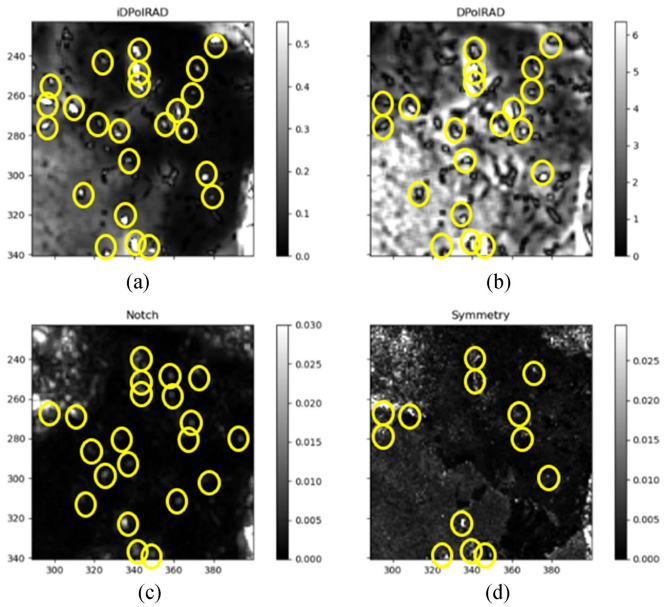

Fig. 5. Contrast image outputs for ROI, April 15th. (a) iDPolRAD. (b) DPolRAD. (c) PNF. (d) Reflection symmetry. Yellow circles indicate the icebergs.

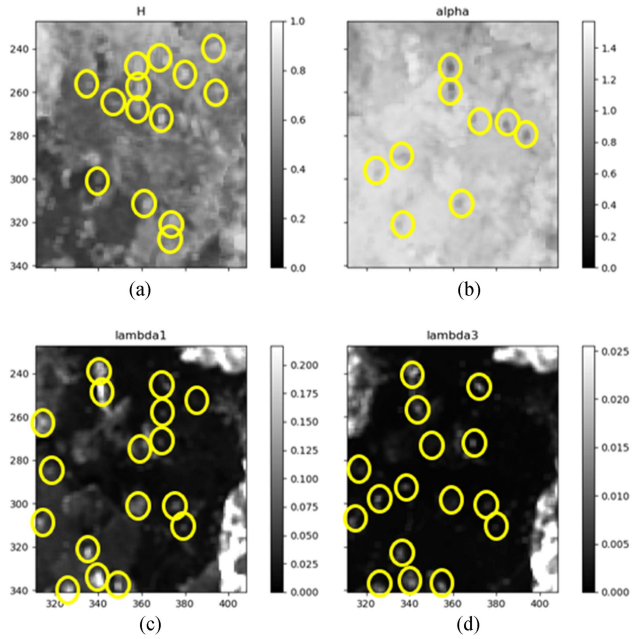

Fig. 6. Contrast image outputs for ROI, April 15th. (a) Entropy. (b) Alpha angle. (c) Lambda1. (d) Lambda3. Yellow circles indicate the icebergs.

is different depending if we focus on low or high value of probability of false alarms.

1) *Low* P_F: The PWF and OPD detectors perform very similarly with P_D values ranging between 0.5 and 0.7 for P_F between 0.01 and 0.1.
2) *High* P_F: When we relax the value for the false alarms to an unrealistic 0.5, the entropy shows the greatest detection performance. Clearly, we are reporting this only for gaining understanding and not suggesting to perform detection with such high P_F.

Entropy is not useful to perform detection with low P_F because sea ice and dark open ocean have large values of entropy. The former is due to the presence of several scattering mechanisms, and the latter is due to the proximity of the noise floor. However, the entropy is also very sensitive to the presence of smaller icebergs because these increase the number of scattering mechanisms in the averaging cell. Therefore, the power of the detector is very high. As a result, when moving to practically unusable level of false alarms, entropy is the only detector that spots the very small icebergs. Overall, it cannot be used as a detector but it helps with understanding the scattering process around icebergs.

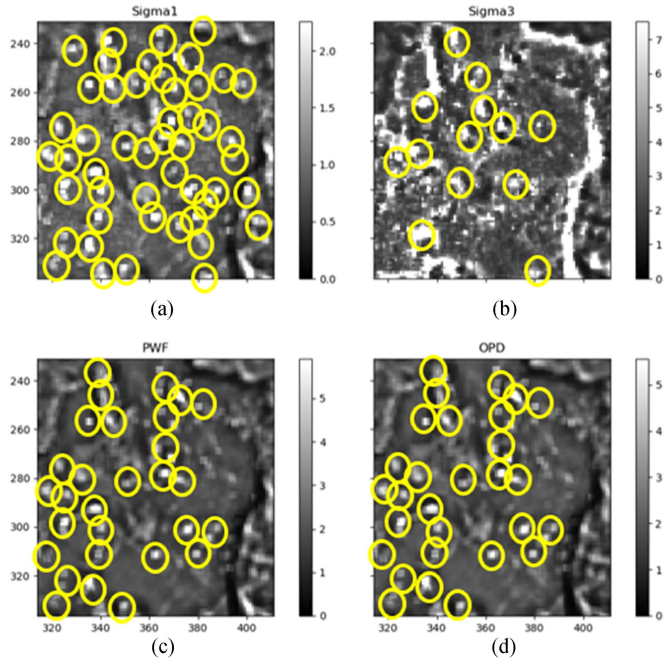

Fig. 7. Contrast image outputs for ROI, April 15th. (a) PMF1. (b) PMF3. (c) PWF. (d) OPD. Yellow circles indicate the icebergs.

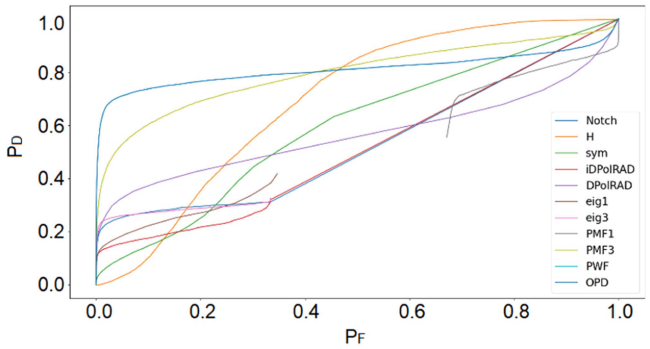

Fig. 8. ROC curves for scene collected 15th April. Notch: PNF; H: entropy; eig1 and eig2: first and third eigenvalues of covariance matrix **[C]**; PMF1 and PMF3: sigma1 and sigma3 of the PMF, i.e., first and last eigenvectors of the optimization; iDPolRAD: dual-intensity polarization ratio anomaly detector; sym: reflection symmetry; PWF: polarimetric whitening filter; and OPD: optimal polarimetric detector.

Fig. 9 shows the ROC curve for the 16th April. Interestingly, the detection performance of the PWF has significantly improved with a P_D value of roughly 0.75 for P_F of 0.01 when compared with the scene collected on 15th April. However, performances of the other detectors, especially of the PMF, PNF, symmetry, eig1, and eig3, have substantially degraded. This is possibly a consequence of a higher sea-state condition on 16th April, producing a more heterogeneous sea surface and increasing the false alarm rate.

Since the PWF detector is not based on contrast enhancement and TCR, but rather speckle reduction, it performs well to the surrounding clutter, suggesting good clutter reduction. A higher increase of sea-state activity and the presence of sea ice explain the degraded performances in the iDPolRAD and DPolRAD detectors, which have low P_D values < 0.4.

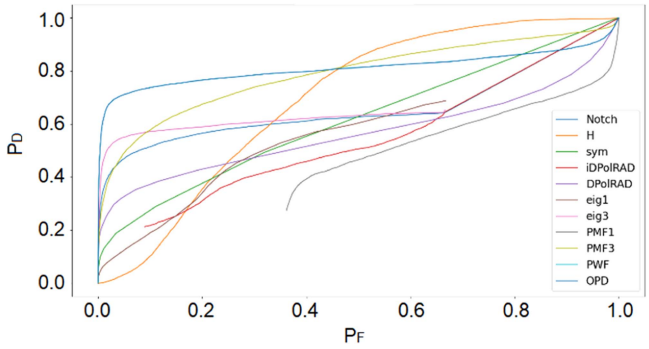

Fig. 9. ROC curves for scene collected 16th April. Notch: PNF; H: entropy; eig1 and eig2: first and third eigenvalues of covariance matrix **[C]**; PMF1 and PMF3: sigma1 and sigma3 of the PMF, i.e., first and last eigenvectors of the optimization; iDPolRAD: dual-intensity polarization ratio anomaly detector; sym: reflection symmetry; PWF: polarimetric whitening filter; and OPD: optimal polarimetric detector.

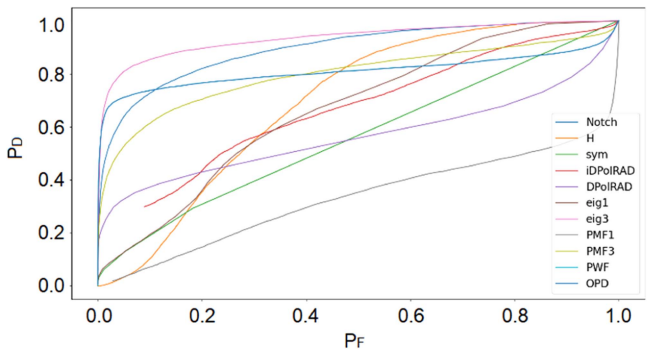

Fig. 10. ROC curves for scene collected 17th April. Notch: PNF; H: entropy; eig1 and eig2: first and third eigenvalues of covariance matrix **[C]**; PMF1 and PMF3: sigma1 and sigma3 of the PMF, i.e., first and last eigenvectors of the optimization; iDPolRAD: dual-intensity polarization ratio anomaly detector; sym: reflection symmetry; PWF: polarimetric whitening filter; and OPD: optimal polarimetric detector.

Fig. 10 presents the ROC for the 17th April acquisition. As in the previous scenes, the OPD and PWF detectors perform incredibly similarly, giving P_D values of roughly 0.7. This is followed by PMF1 and eig1. Here, the eig3 is among one of the top detectors with a P_D of roughly 0.81 when P_F is 0.1.

D. GPRI Detection

As a preliminary analysis, in each ground-radar scene, we consider a few examples of three small icebergs and compare with the satellite data to look for evident differences. Fig. 11 represents four ground and satellite image patches of a particular ROI. In all the corresponding ground-radar images, we can see that the targets are more elongated and stretched in shape when compared with the icebergs in the satellite images. The icebergs in the ground image are also a lot brighter (have a higher contrast) than the ones in the satellite images. This can be attributed to a series of causes.

1) *Higher (grazing) incidence angle in the ground images*: A higher incidence angle may increase the iceberg backscattering by producing more double bounces and, on the other

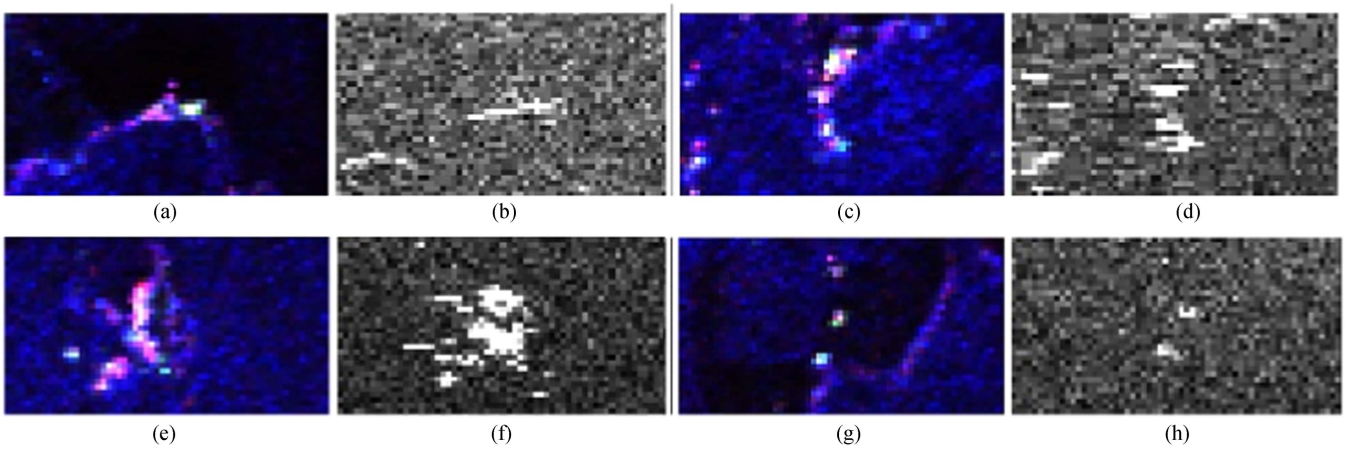

Fig. 11. Iceberg backscattering comparison with satellite and ground radar. (a) Satellite patch and (b) corresponding ground patch with center coordinates 441 411, 8 766 881.2. (c) Satellite patch and (d) corresponding ground patch with center coordinates, 440 732.4, 8 766 551.8. (e) Satellite patch and (f) corresponding ground patch with center coordinates 441 331.1, 8 765 102.4. (g) Satellite patch and (h) corresponding ground patch with center coordinates 441 552.3, 8 765 779, scale is 1:4105, and coordinate reference system is EPSG 32633.

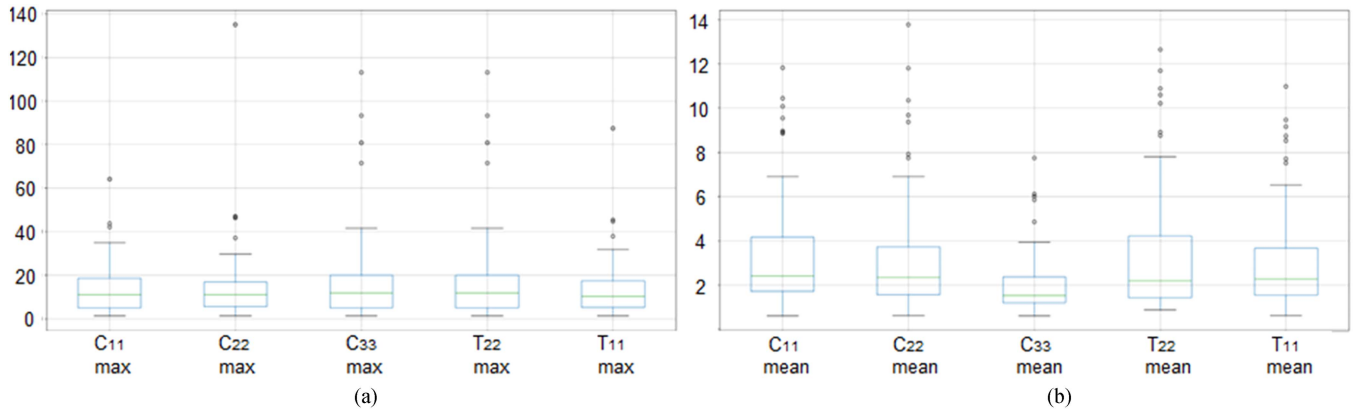

Fig. 12. Satellite TCR. (a) Mean and (b) max boxplots 15th April, plots from left to right: C_{11} channel, C_{22} detector, C_{33} channel, T_{22} channel, and T_{11} channel. Small circles indicate the outliers, green line indicates the average value, and the box shows the interquartile range.

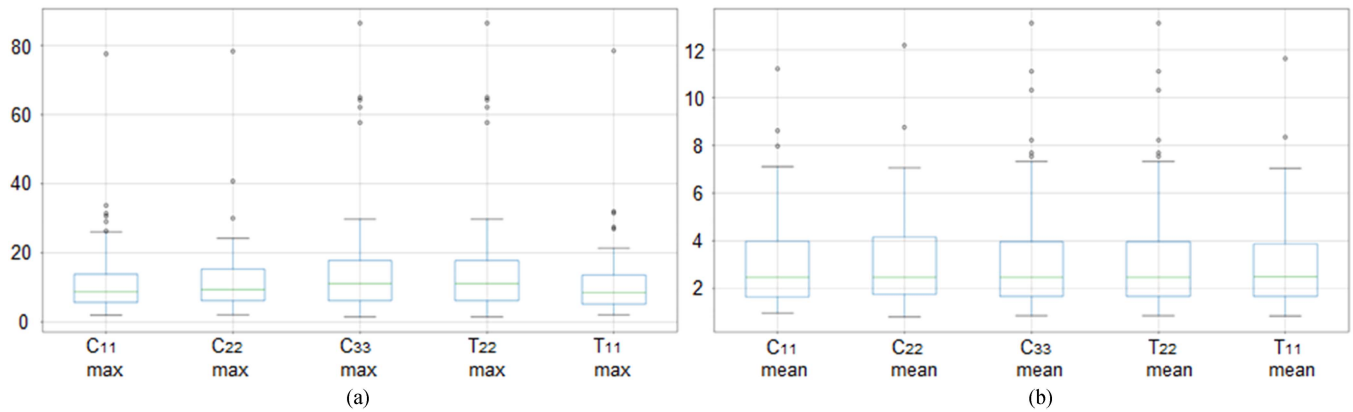

Fig. 13. Satellite TCR. (a) Mean and (b) max boxplots 16th April, plots from left to right: C_{11} channel, C_{22} detector, C_{33} channel, T_{22} channel, and T_{11} channel. Small circles indicate the outliers, green line indicates the average value, and the box shows the interquartile range.

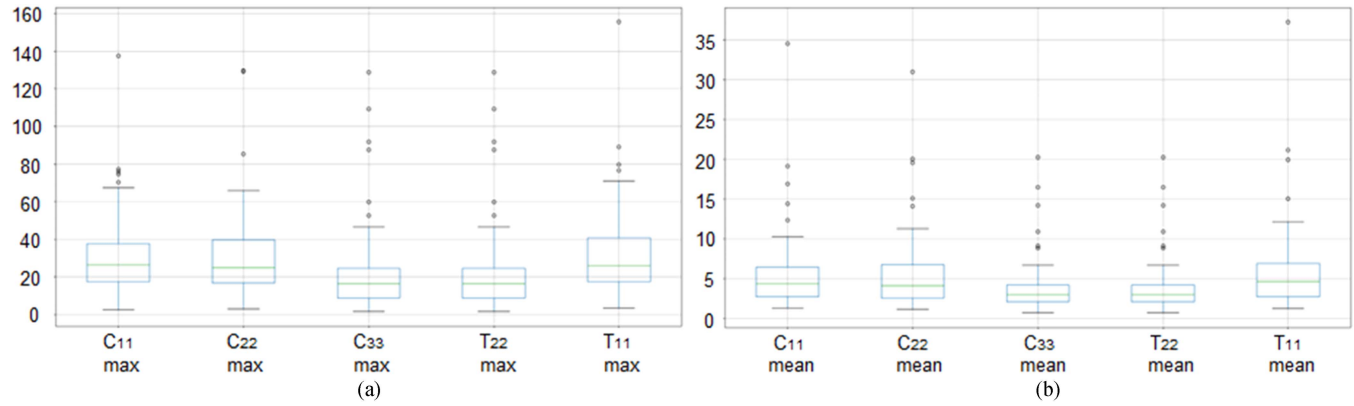

Fig. 14. Satellite TCR. (a) Mean and (b) max boxplots 17th April, plots from left to right: C_{11} channel, C_{22} detector, C_{33} channel, T_{22} channel, and T_{11} channel. Small circles indicate the outliers, green line indicates the average value, and the box shows the interquartile range.

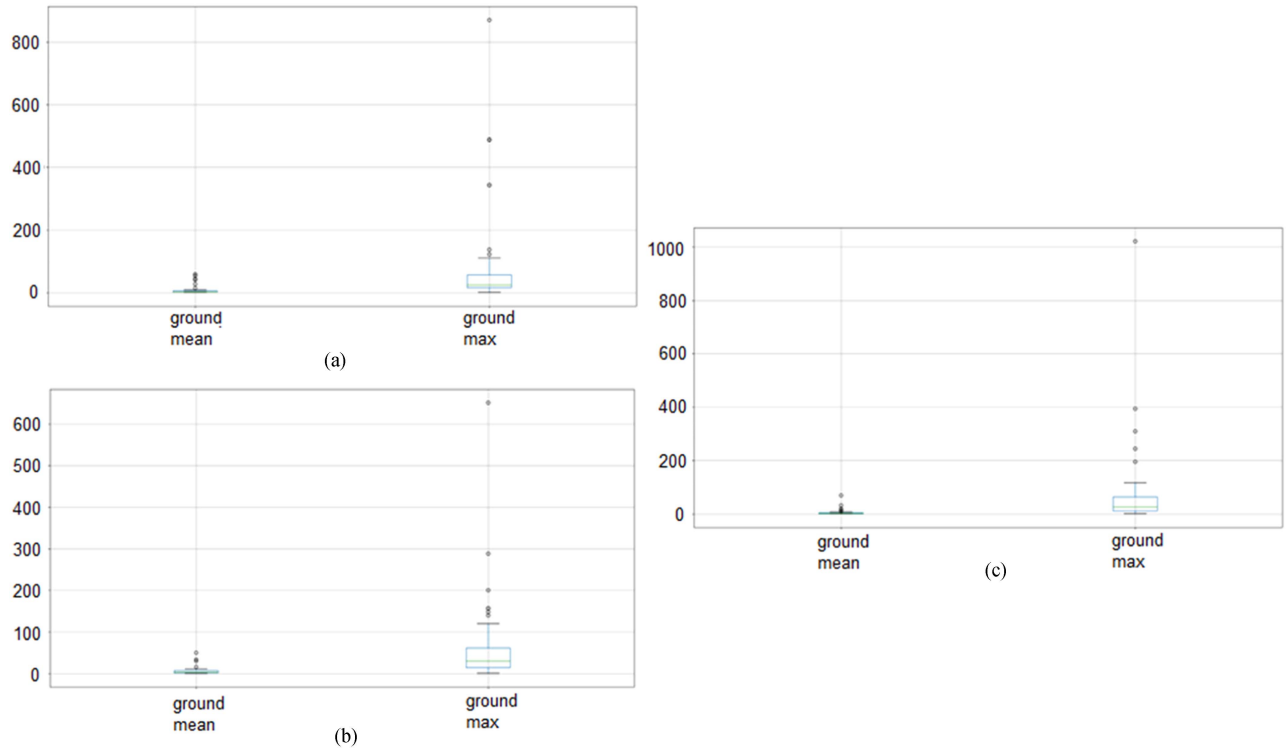

Fig. 15. Ground TCR boxplots. (a) 15th April. (b) 16th April. (c) 17th April, plots from left to right: mean, max. Small circles indicate the outliers, green line indicates the average value, and the box shows the interquartile range.

side, reduce the clutter scattering. However, this will not work if the iceberg is not significantly above the sea level.

2) The across range (the equivalent azimuth for a moving platform) resolution of the ground radar is much larger than the range resolution. This makes the icebergs show more elongated in shape due to the spreading function being so asymmetric.

In Section V-E, we perform a more quantitative comparison between the two systems evaluating the TCR.

E. TCR and Backscattering

Boxplots are presented to show the difference between mean and max TCR values for satellite images (see Figs. 12–14) and ground images (see Fig. 15). In addition to this, we also plotted backscatter values against the area of the icebergs to evaluate if larger icebergs are prone to have larger backscattering. A selection of the scatter plots is presented in Fig. 16. The boxplots are an easy way to represent the different values as observable. They are also more synthetic than using histograms. For the sake of brevity, in this article, we only show scatter plots where the coefficient of correlation between size and backscattering is bigger than 0.5. The plots also include a linear regression to aid the visual interpretation of the data. However, we do not suggest using linear regression to estimate the size of icebergs from backscattering due to the low *R*-squared values. The regression is simply done to provide a numerical way to interpret the cloud of points that are often very clustered or

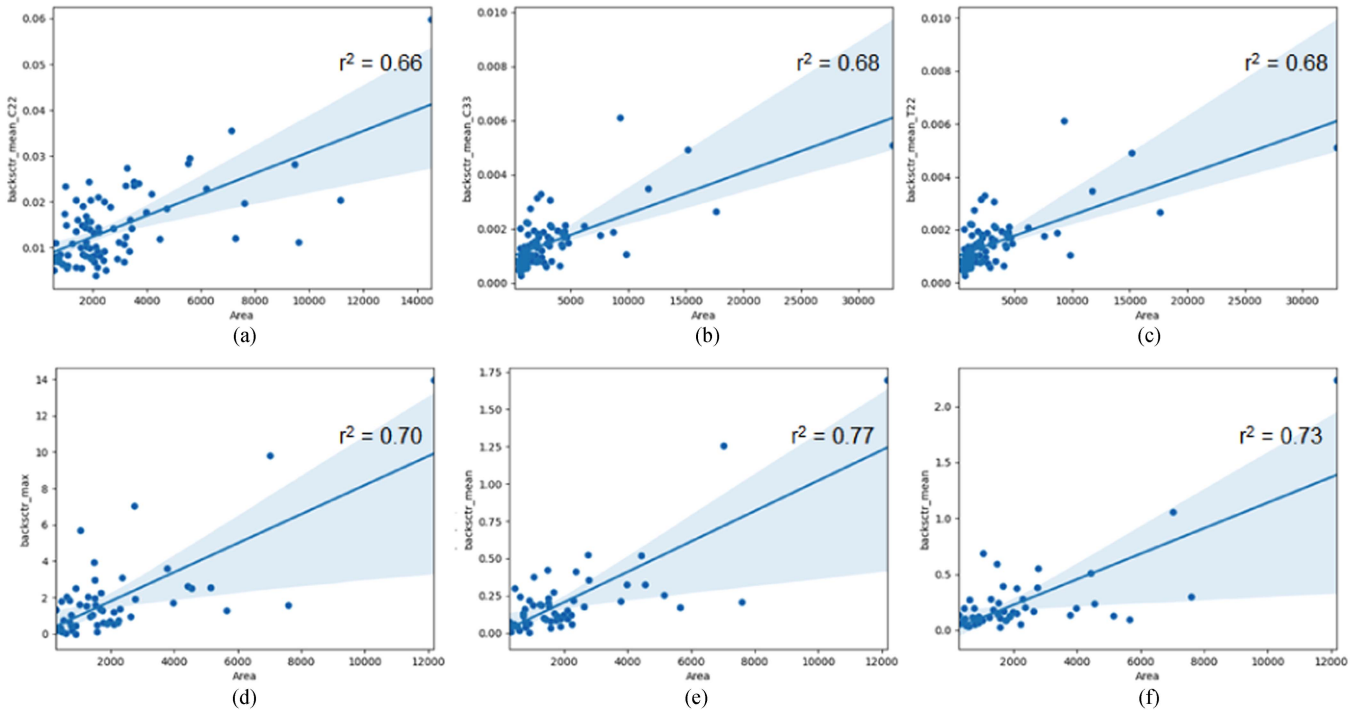

Fig. 16. Iceberg area versus backscatter plots. (a) Mean satellite C_{22} channel 16th April. (b) Mean satellite C_{33} channel 16th April. (c) Mean satellite T_{22} channel 17th April. (d) Max ground 15th April. (e) Mean ground 15th April. (f) Mean ground 17th April. Blue line indicates the linear regression value, and blue area indicates the confidence interval.

not easy to see. The value for the correlation is presented in Table III.

From Fig. 12, we cannot identify any specific pattern for mean TCR. The C_{33} channel appears to remain constant between mean and max TCR. Fig. 13 shows a similar outlook for mean TCR, while the max TCR has increased in range but remained constant across all channels. There are also less outliers for this date. Fig. 14 shows a variation in mean TCR, where the C_{33} and T_{22} channels have a lower range, while the other three channels are constant. The same pattern is found in the max TCR for this date.

VI. Discussion

A. Detection Performance

In Figs. 8–10, the best detection performance on 15th April is from PWF and OPD with $P_D = 0.5$–0.7 for $P_F = 0.01$ and $P_D = 0.75$ for $P_F = 0.05$ on 16th April. The best detection performance on 17th April is from the eig3 with $P_D = 0.81$ for $P_F = 0.1$ followed by the OPD with $P_D = 0.7$ for $P_F = 0.1$. One possible explanation for different performances during the dates is most likely the variation in meteorological conditions. Given that the scene collected on 16th April shows a relatively calmer sea state, the detection is easier. Indeed, previous articles have documented the effect of sea state on detection performance [7], [44]. The entropy interestingly is able to detect most icebergs but at the expense of an unpractical P_F. We find that, although the best detectors are the eig3, PWF, and OPD, they cannot detect 20% of the icebergs. The only way to detect this remaining 20% is to use a detector, such as the entropy, given a higher P_F value of 50%. This is unacceptable for operational use.

B. Target-to-Clutter Ratio

The results of TCR in Figs. 12–15 provide an insight into the separability of target and clutter in backscattering images. The plots show that the majority of icebergs can be easily distinguished from the surrounding open water and sea-ice clutter background, particularly when in the center part of the fjord. However, toward the far inner end of the fjord, icebergs start to meet sea-ice fields as well as smaller fragments of ice broken off the Kongsbreen and Kronebreen glaciers. This may contribute to the huge variation of TCR values seen within the fjord, particularly within the OPD and PWF plots.

When we compare the satellite results to the GPRI results, there are further increased values for the ground radar. A possible reason may be due to the incidence angle, which increased iceberg double bounce and reduced surface scattering from sea and sea ice (see Section V-D). We need also to keep in mind that the frequency is also different, although we would expect that the clutter would be enhanced in the Ku-band by the same amount the icebergs would be.

Interestingly, we find that the TCR values differ depending on each of the polarimetric channels. For example, mean TCR values in the HV and HH channels are roughly similar on 15th April, but HV values are higher on other dates. This is in line with a previous finding, which reported that the cross-polarization channel HV is able to better distinguish icebergs than channels

TABLE IV
BACKSCATTER LINEAR REGRESSION CORRELATION VALUES FOR SATELLITE AND GROUND-BASED RADAR IMAGES

Satellite	**15/04**		**16/04**		**17/04**	
Backscatter	**Max**	**Mean**	**Max**	**Mean**	**Max**	**Mean**
C_{11}	0.27	0.49	0.55	0.64	0.31	0.54
C_{22}	0.25	0.47	0.55	0.66	0.28	0.57
C_{33}	0.20	0.38	0.19	0.38	0.40	0.68
T_{11}	0.30	0.49	0.56	0.65	0.31	0.55
T_{22}	0.20	0.38	0.19	0.38	0.40	0.68
Ground						
TCR	0.70	0.77	0.17	0.50	0.65	0.73

HH and VV due to a lower surface scattering from sea and sea ice found in HV [45].

C. Correlation Between Backscattering and Iceberg Size

The results from the correlation graphs in Fig. 16 and Table IV also suggest that correlation with iceberg size is not straightforward. In the plot, we only listed the few cases where the correlation was higher and it appears that this is the case only when few icebergs have a very large TCR, also leading us to the conclusion that those few realizations may have a very large leverage on the regression (therefore making it not reliable). The linear fit is only for visual aid and we are not proposing this as a valuable scattering model. The correlation using the mean over a small area of the icebergs is generally higher than the one using the maximum inside the same search window. This seems to corroborate the fact that the presence of single bright scatterers on icebergs may be not strongly correlated with the size. The overall size may not be impacting what we see in a small box over the iceberg. Finally, the fact that the correlation is not very high suggests that algorithms to retrieve iceberg size may be better directed to extract dimensions using some computer vision methodology rather than regressing based on backscattering values.

Backscatter correlation with iceberg size is shown to be higher in ground images, as a result of a shallower incidence angle. Since the main scattering mechanism here is likely to be the double bounce, a larger iceberg may imply a larger position above the water and, therefore, a bigger double bounce. This was less visible using satellite data due to the different incidence angles.

D. Satellite and Ground Comparison

The use of ground data in this work allows for validating the results, as well as comparing the outputs in Figs. 11–16. Looking at the visual comparison in Fig. 11, it is clear that both the ground and satellite images show the same icebergs in the area and that visual inspection of icebergs in both data types is possible. However, owing to a shallower incidence angle, the icebergs in the ground images are more elongated in shape. Unfortunately, the ground radar did not acquire polarimetric information, so we were unable to comment on that. The higher resolution and the more beneficial geometry may provide some advantages for the use of ground radar, when this is available (e.g., near coast like). But this is obviously not possible in the middle of the ocean where the height of the vessel is not large enough to take the advantage of double bounce from the sea surface, which is very small for incidence angles close to 90°.

E. Contribution

The nature of this study provided important requirements for the use of the ground radar. The topography and location of the ground radar allowed for the ideal incidence angle range to look for icebergs. This is because the radar does not perform well with an incidence angle that is very shallow, as the pulse would not be scattered back to the antenna since the shape of the icebergs would allow the pulse to behave in a stealth-like manner. Similarly, an incidence angle that is closer to 0° might have too much return from the sea surface. Given the behavior of seawater, a Bragg-type scattering may simply scatter too much from the sea. Where possible, we suggest that ground radars be installed at elevation that will allow an incidence angle, which is shallow, but not 90°, validating small iceberg sightings.

F. Limitations

The methods presented in this section are open to a few limitations. The calculation for iceberg area may not reflect actual surface area because of SAR distortions/smearing. Previous work by [25] shows that iceberg area is also calculated using the same approach. To avoid this problem, working with different incidence angles may be an option. It may be possible to identify the same iceberg in differing images that are acquired with different incidence angles, and then take the average area for each iceberg to account for various SAR distortions. However, this may not be practical. Another option would be including a step-in image processing that corrects geometrical distortions caused by differing incidence angles.

The meteorological data obtained for this work are limited in which it was only available on an hourly basis. Wind speed and direction can change very quickly, and this can influence detection results.

VII. CONCLUSION

In this work, we tested six state-of-the-art detectors with both an RS2 and GPRI dataset on icebergs in Kongsfjorden, Svalbard. These detectors are the iDPoLRAD and DPoLRAD, PNF, PMF, reflection symmetry (sym), PWF, and OPD. Detection performance was estimated over three quad-polarimetric *C*-band RS2 SLC images, each collected between 15th and 17th April 2016. To validate the data, we also use three GPRI images of the same area, collected synchronously. We show that the OPD and PWF detectors provide the best detection performance, even when factors, such as sea-ice cover, sea state, and homogeneity, are considered. P_D values range from 0.5 to 0.7 on 15th April during a choppy sea state for a P_F of 0.01 and to 0.75 on 16th for a P_F of 0.05. On 17th April, where the sea is calmer, the

eig3 shows the best performance with a P_D of 0.81 when the P_F is 0.1. These high levels of false alarms are the witness of the difficulty of detecting small icebergs in sea ice and further future work will be needed to improve this, potentially by using higher resolution images. TCR values showed major variation because of factors, such as polarimetric channels, window size of pixel area, and sea-ice activity toward the inner part of the fjord. Overall, this study contributes the potential of PolSAR data to identify icebergs in interchangeable and challenging conditions. Given that the limitations of this work include small incidence angles, future work could be focused on the use of higher incidence angles to compare multiple scattering mechanisms in the area. Owing to a progression in the abundance of data now made available from future SAR missions with wider swath widths and finer spatial resolutions, the use of machine learning and computer vision techniques are being utilized within iceberg detection. Wider swath widths will lead to more frequent acquisitions. The combination of detector algorithms and advanced machine learning, such as convolutional neural networks, has the potential to show increased detector performance, given that a large amount of training and testing data can now be achieved.

ACKNOWLEDGMENT

RS-2 data were provided by NSC/KSAT under the Norwegian/Canadian Radarsat Agreement 2016. Data were preprocessed at CIRFA UiT-The Arctic University of Norway and only multilooked geocoded products were used outside UiT.

REFERENCES

[1] G. R. Bigg, *Icebergs: Their Science and Links to Global Change*. Cambridge, U.K.: Cambridge Univ. Press, 2015.

[2] A. Marino and I. Hajnsek, "Icebergs detection with TerraSAR-X data using a polarimetric notch filter," in *Proc. IEEE Int. Geosci. Remote Sens. Symp.*, Munich, Germany, 2012, pp. 3273–3276.

[3] C. Wesche and W. Dierking, "Iceberg signatures and detection in SAR images in two test regions of the Weddell Sea, Antarctica," *J. Glaciol.*, vol. 58, no. 208, pp. 325–339, 2012.

[4] W. Dierking and C. Wesche, "C-band radar polarimetry—Useful for detection of icebergs in sea ice?," *IEEE Trans. Geosci. Remote Sens.*, vol. 52, no. 1, pp. 25–37, Jan. 2014.

[5] I. Zakharov, D. Power, P. Bobby, and C. Randell, "Multi-resolution SAR data analysis for automated retrieval of sea ice and iceberg parameters," in *Proc. ESA Living Planet Symp.*, 2013.

[6] A. Frost, R. Ressel, and S. Lehner, "Automated iceberg detection using high-resolution X-band SAR images," *Can. J. Remote Sens.*, vol. 42, no. 4, pp. 354–366, 2016.

[7] V. Akbari and C. Brekke, "Iceberg detection in open water and sea ice using C-band radar polarimetry," in *Proc. IEEE Int. Geosci. Remote Sens. Symp.*, Fort Worth, TX, USA, 2017, pp. 2298–2301.

[8] F. Nunziata, A. Buono, M. Migliaccio, M. Moctezuma, F. Parmiggiani, and G. Aulicino, "Multi-frequency and multi-polarization synthetic aperture radar for the Larsen-C A-68 iceberg monitoring," in *Proc. IEEE 4th Int. Forum Res. Technol. Soc. Ind.*, Palermo, Italy, 2018, pp. 1–4.

[9] I. H. Soldal, W. Dierking, A. Korosov, and A. Marino, "Automatic detection of small icebergs in fast ice using satellite wide-swath SAR images," *Remote Sens.*, vol. 11, no. 7, 2019, Art. no. 806.

[10] H. Heiselberg, "Ship-iceberg classification in SAR and multispectral satellite images with neural networks," *Remote Sens.*, vol. 12, no. 15, 2020, Art. no. 2353.

[11] S. Gerland and A. H. Renner, "Sea-ice mass-balance monitoring in an Arctic fjord," *Ann. Glaciol.*, vol. 46, pp. 435–442, 2007.

[12] J. A. Dowdeswell and M. O. Jeffries, "Arctic ice shelves: An introduction," in *Arctic Ice Shelves and Ice Islands*. Berlin, Germany: Springer, 2017, pp. 3–21.

[13] R. May et al., "Morphometry and mass of icebergs in the Russian Arctic Seas," *Int. J. Offshore Polar Eng.*, vol. 29, no. 4, pp. 375–382, 2019.

[14] Y. A. Romanov, N. A. Romanova, and P. Romanov, "Geographical distribution and volume of Antarctic icebergs derived from ship observation data," *Ann. Glaciol.*, vol. 58, no. 74, pp. 28–40, 2017.

[15] C. Wesche and W. Dierking, "Near-coastal circum-Antarctic iceberg size distributions determined from synthetic aperture radar images," *Remote Sens. Environ.*, vol. 156, pp. 561–569, 2015.

[16] N. Young, D. Turner, G. Hyland, and R. Williams, "Near-coastal iceberg distributions in East Antarctica, 50-145 E," *Ann. Glaciol.*, vol. 27, pp. 68–74, 1998.

[17] C. Oliver and S. Quegan, *Understanding Synthetic Aperture Radar Images*. Tambaram, India: SciTech Publishing, 2004.

[18] D. Tao, S. N. Anfinsen, and C. Brekke, "Robust CFAR detector based on truncated statistics in multiple-target situations," *IEEE Trans. Geosci. Remote Sens.*, vol. 54, no. 1, pp. 117–134, Jan. 2016.

[19] T. Li, D. Peng, Z. Chen, and B. Guo, "Superpixel-level CFAR detector based on truncated gamma distribution for SAR images," *IEEE Geosci. Remote Sens. Lett.*, vol. 18, no. 8, pp. 1421–1425, Aug. 2021.

[20] D. Tao, A. P. Doulgeris, and C. Brekke, "A segmentation-based CFAR detection algorithm using truncated statistics," *IEEE Trans. Geosci. Remote Sens.*, vol. 54, no. 5, pp. 2887–2898, May 2016.

[21] J. Bailey, A. Marino, and V. Akbari, "Comparison of target detectors to identify icebergs in quad-polarimetric L-band synthetic aperture radar data," *Remote Sens.*, vol. 13, no. 9, 2021, Art. no. 1753.

[22] D. J. Crisp, "The state-of-the-art in ship detection in synthetic aperture radar imagery," Defence Sci. Technol. Org., Salisbury, U.K., 2004.

[23] J. Karvonen, A. Gegiuc, T. Niskanen, A. Montonen, J. Buus-Hinkler, and E. Rinne, "Iceberg detection in dual-polarized C-band SAR imagery by segmentation and nonparametric CFAR (SnP-CFAR)," *IEEE Trans. Geosci. Remote Sens.*, vol. 60, Apr. 2021, Art. no. 4300812.

[24] A. Marino, W. Dierking, and C. Wesche, "A depolarization ratio anomaly detector to identify icebergs in sea ice using dual-polarization SAR images," *IEEE Trans. Geosci. Remote Sens.*, vol. 54, no. 9, pp. 5602–5615, Sep. 2016.

[25] V. Akbari and C. Brekke, "Iceberg detection in open and ice-infested waters using C-band polarimetric synthetic aperture radar," *IEEE Trans. Geosci. Remote Sens.*, vol. 56, no. 1, pp. 407–421, Jan. 2018.

[26] U. H. Himi, M. S. Ferdous, D. T. Power, and P. McGuire, "Statistical comparison of melting iceberg backscatter embedded in sea ice and open water using RADARSAT-2 images of the Newfoundland sea," *IEEE Trans. Geosci. Remote Sens.*, vol. 60, Sep. 2021, Art. no. 5212213.

[27] C. Werner, T. Strozzi, A. Wiesmann, and U. Wegmüller, "GAMMA's portable radar interferometer," in *Proc. 13th FIG Symp. Deform. Meas. Anal.*, 2008, pp. 1–10.

[28] C. Werner, A. Wiesmann, T. Strozzi, A. Kos, R. Caduff, and U. Wegmiüler, "The GPRI multi-mode differential interferometric radar for ground-based observations," in *Proc. 9th Eur. Conf. Synthetic Aperture Radar*, 2012, pp. 304–307.

[29] S. Cloude, *Polarisation: Applications in Remote Sensing*. London, U.K.: Oxford Univ. Press, 2010.

[30] J.-S. Lee and E. Pottier, *Polarimetric Radar Imaging: From Basics to Applications*. Boca Raton, FL, USA: CRC press, 2017.

[31] S. Brusch, S. Lehner, T. Fritz, M. Soccorsi, A. Soloviev, and B. van Schie, "Ship surveillance with TerraSAR-X," *IEEE Trans. Geosci. Remote Sens.*, vol. 49, no. 3, pp. 1092–1103, Mar. 2011.

[32] A. Marino, "A notch filter for ship detection with polarimetric SAR data," *IEEE J. Sel. Topics Appl. Earth Observ. Remote Sens.*, vol. 6, no. 3, pp. 1219–1232, Jun. 2013.

[33] L. M. Novak, M. B. Sechtin, and M. J. Cardullo, "Studies of target detection algorithms that use polarimetric radar data," *IEEE Trans. Aerosp. Electron. Syst.*, vol. 25, no. 2, pp. 150–165, Mar. 1989.

[34] F. Nunziata, M. Migliaccio, and C. E. Brown, "A physically-based approach to observe man-made metallic objects in dual-polarized SAR data," in *Proc. IEEE Int. Geosci. Remote Sens. Symp.*, Honolulu, HI, USA, 2010, pp. 3007–3010.

[35] L. M. Novak and M. C. Burl, "Optimal speckle reduction in POL-SAR imagery and its effect on target detection," in *Proc. Millimeter Wave Synthetic Aperture Radar*, 1989, pp. 84–115.

[36] G. Liu, S. Huang, A. Torre, and F. Rubertone, "The multilook polarimetric whitening filter (MPWF) for intensity speckle reduction in polarimetric SAR images," *IEEE Trans. Geosci. Remote Sens.*, vol. 36, no. 3, pp. 1016–1020, May 1998.
[37] V. Akbari, C. Brekke, A. P. Doulgeris, R. Storvold, and A. H. Sivertsen, "Quad-polarimetric SAR for detection and characterization of icebergs," in *Proc. ESA Living Planet Symp.*, Prague, Czech Republic, 2016, pp. 1–8.
[38] A. Cristea, A. P. Doulgeris, and T. Eltoft, "A filtering framework for SAR data based on nongaussian statistics and pixel clustering," in *Proc. Image Signal Process. Remote Sens. XXIII*, 2017, Paper 1042713.
[39] H. Svendsen et al., "The physical environment of Kongsfjorden–Krossfjorden, an Arctic fjord system in Svalbard," *Polar Res.*, vol. 21, no. 1, pp. 133–166, 2002.
[40] J. A. Dowdeswell and C. F. Forsberg, "The size and frequency of icebergs and bergy bits derived from tidewater glaciers in Kongsfjorden," *Northwest Spitsbergen. Polar Res.*, vol. 11, no. 2, pp. 81–91, 1992.
[41] O. Liestøl, "The glaciers in the kongsfjorden area spitsbergen," *Norsk Geografisk Tidsskrift-Norwegian J. Geography*, vol. 42, no. 4, pp. 231–238, 1988.
[42] J. A. Dowdeswell, "On the nature of svalbard icebergs," *J. Glaciology* vol. 35, no. 120, pp. 224–234, 1989.
[43] C. Livingstone, I. Sikaneta, C. Gierull, S. Chiu, and P. Beaulne, "RADARSAT-2 system and mode description," Defence Res. Develop. Canada, Ottawa, ON, Canada, 2006.
[44] M. M. Barbat, C. Wesche, A. V. Werhli, and M. M. Mata, "An adaptive machine learning approach to improve automatic iceberg detection from SAR images," *ISPRS J. Photogramm. Remote Sens.*, vol. 156, pp. 247–259, 2019.
[45] J. Bailey and A. Marino, "Quad-polarimetric multi-scale analysis of icebergs in ALOS-2 SAR data: A comparison between icebergs in West and East Greenland," *Remote Sens.*, vol. 12, no. 11, 2020, Art. no. 1864.

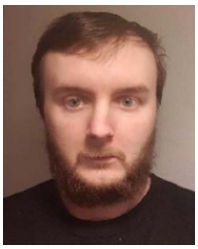

Johnson Bailey (Member, IEEE) received the M.Sc. degree in geological and environmental hazards from the University of Portsmouth, Portsmouth, U.K., in 2016, and the Ph.D. degree in environmental science, with a thesis on polarimetric SAR analysis of icebergs from the Faculty of Natural Sciences, University of Stirling, Stirling, U.K., in 2023.

Since 2024, he has been a Senior Research Associate in iceberg detection and commercialization with Lancaster University, Department of Physics, Lancaster, U.K. His research interests include SAR polarimetry, iceberg physics, computer vision, and machine learning/deep learning for iceberg detection and classification using radar remote sensing data.

Vahid Akbari received the Ph.D. degree in physics with a specialization in radar remote sensing and data analytics from the UiT—The Arctic University of Norway, Tromsø, Norway, in 2013.

Since 2014, he continued his research in radar remote sensing and machine learning as a Postdoctoral Research Fellow with the UiT—The Arctic University of Norway, the Norwegian Institute of Bioeconomy Research, Akershus, Norway, and the University of Stirling, Stirling, U.K. He was a Visiting Scientist with Signal Processing and Telecommunications Laboratory, Department of Electrical, Electronic, Telecommunications Engineering and Naval Architecture, University of Genoa, Genoa, Italy, in 2011, and a Visiting Researcher with the German Geoscience Centre, Potsdam, Germany, in 2008. He was an Assistant Professor with the University of Tehran in 2015. Since 2023, he has been a Lecturer (Assistant Professor) in data science/artificial intelligence with the University of Stirling. His primary research interests revolve around the intersection of radar remote sensing and statistical modeling/machine learning, with a particular focus on the applications in environmental monitoring.

Tao Liu (Member, IEEE) received the B.S. degree in communication engineering and the Ph.D. degree in information and communication engineering from the National University of Defense Technology, Changsha, China, in 2001 and 2007, respectively.

In 2000, he was the Outstanding Communist Youth League member of China. Since 2007, he has been with the School of Electronic Engineering, Naval University of Engineering, Wuhan, China, where he is currently a Professor.

Dr. Liu was a recipient of the Award of Excellent Doctor Thesis of Chinese Army in 2009. Since 2019, he has been a committee member in the Radar Society of the Chinese Institute of Electronics. He has authored more than 50 journal papers and 3 books. His research interests include statistical theory of radar polarization, polarization information processing, synthetic aperture radar (SAR) automatic target recognition, statistical modeling of SAR image, SAR ship detection, interferometric SAR, SAR ground moving target indication, and artificial intelligence.

Tom Rune Lauknes (Member, IEEE) received the Ph.D. in physics from the University of Tromsø, Tromsø, Norway, in 2011.

His major field of study is satellite and airborne remote sensing, with a specific focus on synthetic aperture radar (InSAR) applications in the Arctic and polar regions. Since 2005, he has been with Norut, now known as NORCE Norwegian Research Centre, Bergen, Norway, where he holds the position of Senior Research Scientist, based in Tromsø, Norway. He possesses extensive experience in using terrestrial, airborne, and satellite radar and optical remote sensing methods, for monitoring landslides and periglacial landforms, such as rock glaciers, extending to polar research, particularly in monitoring Arctic sea ice and calving glaciers. He has contributed significantly to the InSAR Norway project. His past roles include being a Visiting Researcher with Radar Interferometry Group, Stanford University, in 2007 and 2008, a Visiting Research Fellow with the Centre for Space Research, University of Texas at Austin in 2010, and a Visiting Scholar with the Department of Geography, University of California, Santa Barbara, in 2014.

Armando Marino (Member, IEEE) received the M.Sc. degree in telecommunication engineering from the Universita' di Napoli "Federico II," Naples, Italy, in 2006, and the Ph.D. degree in polarimetric SAR interferometry from the School of Geosciences, University of Edinburgh, Edinburgh, U.K., in 2011.

In 2006, he joined High Frequency and Radar Systems Department, German Aerospace Centre, Oberpfaffenhofen, Germany, where he developed the M.Sc. thesis. From March 2011 to October 2011, he was with the University of Alicante, Institute of Computing Research, Spain. From 2011 to 2015, he was a Postdoctoral Researcher and a Lecturer with ETH Zurich, Institute of Environmental Engineering, Switzerland. Since 2015, he has been a Lecturer with the School of Engineering and Innovation, Open University, Milton Keynes, U.K. Since 2018, he has been an Associate Professor with the Faculty of Natural Sciences, University of Stirling, Stirling, U.K.